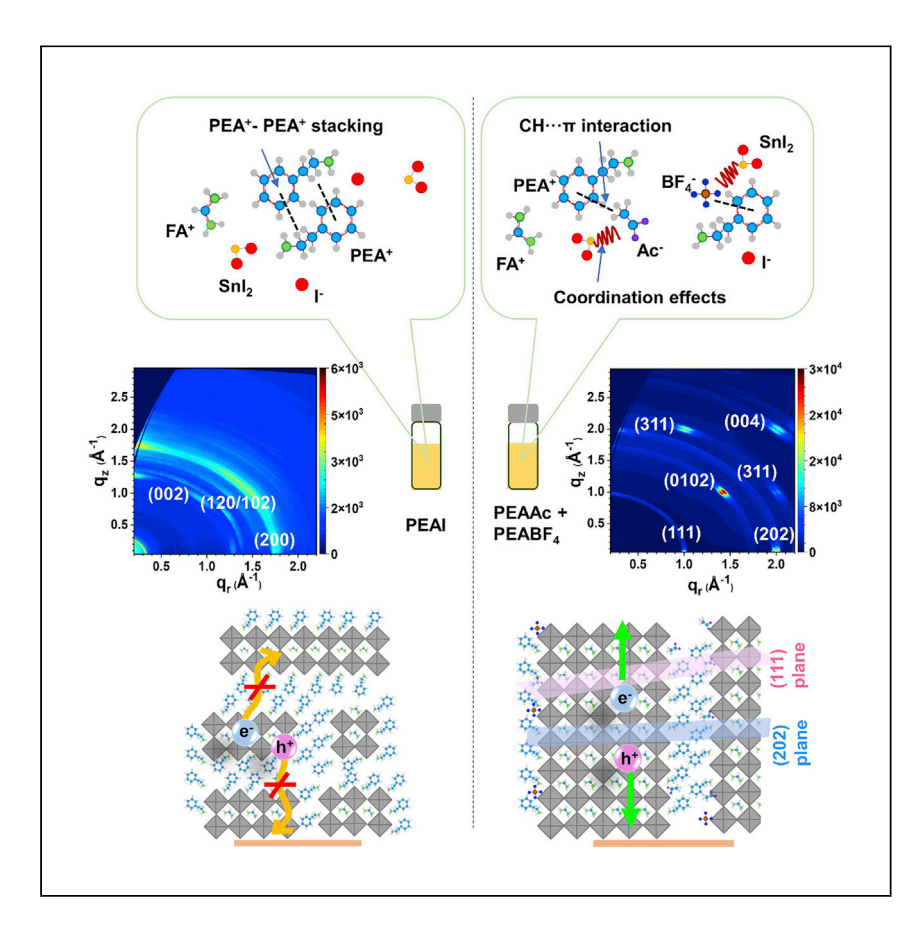




Article

Pseudo-halide anion engineering for efficient quasi-2D Ruddlesden-Popper tin perovskite solar cells



The poor stability of tin perovskites greatly hinders their photovoltaic applications. Li et al. propose a pseudo-halide engineering strategy to grow 2D Ruddlesden-Popper tin perovskites with reduced small n-value 2D phases and improved crystal orientation. Efficiency up to 9% and 400 h stability is achieved.

Hao Li, Yuanze Xu, Shripathi Ramakrishnan, Yugang Zhang, Mircea Cotlet, Tony Lou Xu, Qiuming Yu

qy10@cornell.edu

Highlights

Efficiency up to 9% is achieved for 2D tin perovskite solar cells with good stability

The crystallization process is successfully controlled by pseudo-halide engineering

Vertical orientation and reduced small n-value 2D phases are achieved

Li et al., Cell Reports Physical Science 3, 101060 October 19, 2022 © 2022 The Author(s). https://doi.org/10.1016/j.xcrp.2022.101060



Article

Pseudo-halide anion engineering for efficient quasi-2D Ruddlesden-Popper tin perovskite solar cells

Hao Li,¹ Yuanze Xu,¹ Shripathi Ramakrishnan,¹ Yugang Zhang,² Mircea Cotlet,² Tony Lou Xu,¹ and Qiuming Yu^{1,3,*}

SUMMARY

Quasi-two-dimensional (2D) organic-inorganic hybrid tin perovskites have emerged as promising alternatives to lead-based perovskites in thin-film photovoltaics because of their reduced toxicity and improved stability. However, the undesired small n-value 2D phases and disordered crystal orientation enormously restrict the efficiency of quasi-2D tin perovskite solar cells (PSCs) due to uncontrollable nucleation and crystal growth processes. Here, we propose a mixed pseudo-halide anion engineering approach by using acetate (Ac⁻) and tetrafluoroborate (BF₄⁻) anions to make quasi-2D Ruddlesden-Popper perovskites with a target formula of PEA₂FA₄ Sn₅I₁₆. We find that the mixed Ac⁻ and BF₄⁻ anions can not only promote homogeneously distributed PEA⁺ cations in the precursor by effectively breaking the PEA+...PEA+ stacking but also retard the crystallization process by coordinating with unbonded SnI₂, thereby, significantly reducing small n-value 2D phases, improving the crystal orientation, and suppressing the Sn²⁺ oxidation. The resulting PSC exhibits up to 9% power conversion efficiency and 400 h stability.

INTRODUCTION

Hybrid organic-inorganic lead halide perovskite solar cells (PSCs) have emerged in the past decade as a promising low-cost, thin-film solar cell with power conversion efficiency (PCE) increasing from 3.8% to 25.6%^{1,2} and the potential for roll-to-roll printing capabilities,³ creating a competitive cost for energy, which could encourage a transition into a clean energy economy. The most efficient PSCs are using Pb-based perovskites, which raises some concerns for commercialization because of the potential environmental contamination and human health problems.^{4,5} For large-scale commercialization of halide PSCs, even with rigorous industrial hygiene program and encapsulation of solar module, the lead ion still could leakage to the environment during the whole products life cycle. Therefore, it is important to carefully find an environmentally benign and efficient replacement for Pb with a focus on keeping the excellent properties ascribed to its presence in perovskite compounds.

So far, a variety of efforts have been applied to replace lead perovskite with non-toxicity compounds such as tin (Sn), ⁴ germanium (Ge), ⁶ copper (Cu), ⁷ antimony (Sb), ⁸ or bismuth (Bi). ⁹ Among those candidates, tin perovskite is regarded as an ideal candidate to replace lead perovskite due to its narrow bandgap (~1.2–1.4 eV), greater charge-carrier mobility and environmentally benign character. ^{10,11} Up to now, tin PSCs demonstrate the highest efficiency among all kinds of lead-free

¹Robert Frederick Smith School of Chemical and Biomolecular Engineering, Cornell University, Ithaca, NY, USA

²Center for Functional Nanomaterials, Brookhaven National Laboratory, Upton, NY, USA

³Lead contact

^{*}Correspondence: qy10@cornell.edu https://doi.org/10.1016/j.xcrp.2022.101060



Cell Reports
Physical Science
Article

perovskites. 12,13 The challenge with Sn-based PSCs is primarily related to the difficulty in controlling Sn defects, in particular Sn vacancies in 3D tin perovskite. 13 Sn vacancies form and diffuse relatively easily, resulting in the undesirable nonradiative recombination of photocarriers, metallic conductivity, and the attendant loss of open-circuit voltage, V_{OC} . In addition, the dangling bonds on the surface and at the grain boundaries introduce trap states, which act as the centers of nonradiative recombination and degradation sites.

Two-dimensional (2D) perovskites are more stable than 3D perovskites because the bulky organic cations protect the inorganic perovskite slabs from moisture and minimize ion migration. 14-16 Hence, it opens a promising avenue to achieve high performance tin-based PSCs with better stability. The Ruddlesden-Popper (RP) phase 2D perovskite has a formula of $A'_2A_{n-1}Sn_nX_{3n+1}$, where A' is a bulky organic monoammonium cation, A is a small monovalent cation, X is a halide anion, and n represents the number of SnX_6 octahedral layers that are separated by the large A'-site cations. The n = 1 of the perovskites is regarded as ideal 2D octahedral layers. By increasing the thickness of the octahedral layers (n > 1), the so-called quasi-2D structure is obtained. ¹⁷ Bulky monoammonium cations such as butylammonium (BA⁺) ¹⁸ and phenylethylammonium (PEA⁺)^{19,20} are commonly incorporated into formamidinium tin triiodide (FASnI₃) or methylammonium tin triiodide (MASnI₃) to form either 2D/3D bulk heterojunction (BHJ) structures or 2D/3D planar heterojunction (PHJ) structures in the tin perovskite thin films. The advantages of 2D/3D BHJ structures include wellpassivated grains by bulky cations across the whole film, decreased trap states, and improved stability. Nevertheless, charge transfer between inorganic slabs may be disrupted by the bulky cation layer. ^{18,21} While 2D/3D PHJ structures have the benefit of preserving the excellent electronical characteristics of 3D perovskites and enhancing the stability enabled by the encapsulation of film surfaces by 2D phases, a large number of trap states may still exist in the 3D perovskites. 22,23 Recently, significant efforts have been made to manipulate the 2D/3D BHJ and PHJ structured tin perovskites to increase their efficiency and stability concurrently, e.g., forming 2D RP tin perovskites over 3D tin perovskites¹⁹ or 2D Dion-Jacobson phase at the grain boundaries of 3D tin perovskite, 24 applying SnF₂ additives, 25,26 and adding antioxidation agents to reduce Sn²⁺ oxidation and to passivate grain boundary defects.²⁷⁻²⁹ However, simultaneously achieving both long-term stability and high efficiency remains a significant challenge.

Quasi-2D Sn perovskites, without 3D structures, show promise for obtaining both high stability and efficiency as compared with 2D/3D BHJ and PHJ structures. Even though a relative low PCE of 2.5% was achieved for PSCs based on guasi-2D Sn RP phase perovskite thin films made from pre-synthesized BA₂MA₃Sn₄I₁₃ (n = 4) single crystals, the PSCs retained 90% initial PCE for 30 days with encapsulation.³⁰ The efforts using ammonium chloride as additive to prepare AVA₂FA_{n-1}Sn_n I_{3n+1} (<n> = 5) thin films, where AVA is 5-ammonium valeric acid, achieved a PCE of 8.7% with almost no performance decrease for over 400 h.³¹ Cation engineering was applied to prepare $(BA_{0.5}PEA_{0.5})_2FA_3Sn_4I_{13}$ quasi-2D (n = 4) tin perovskite thin films.³² The morphology and crystal orientation of thin films were greatly improved, resulting in a PCE of 8.82% and a retention of 60% initial performance for 25 days. However, there is no efficiency breakthrough for quasi-2D Sn perovskite PSCs compared with their counterparts with 2D/3D BHJ or PHJ structured Sn perovskites, whose best PCE is 14.6%.³³ The challenges come from the difficult in controlling guasi-2D phase distribution and crystal orientation in the active layers. The crystal growth speed of small n-value phases is generally slower than larger n-value phases. This growth speed difference physically brings competitive growth between

Article



different phases at different depths of thin films, which results in small grain size, random orientation, and disordered structure. Substituting halide I⁻ with pseudohalide anions, e.g., acetate (CH₃COO⁻, Ac⁻), ³³ formate (HCOO⁻), ^{34,35} and thiocyanate (SCN⁻), ¹⁹ or chloride (CI⁻), ³⁶ has been demonstrated to be an effective way to address the fast crystal growth in both lead and tin-based perovskites. ^{37–43} Furthermore, these anions have the potential to form strong ionic interactions with the perovskite framework, lowering trap states and boosting device stability. Therefore, it is promising to apply anion engineering in controlling quasi-2D tin perovskite growth and orientation.

We propose a mixed pseudo-halide engineering approach by using acetate (Ac⁻) and tetrafluoroborate (BF₄⁻) anions to pair with PEA⁺ cations as PEAAc and PEABF₄ instead of the conventional iodide anion (I⁻) as PEAI for the formation of quasi-2D tin perovskite $PEA_2FA_4Sn_5I_{16}$ (<n> = 5). Using pseudo-halides offers the following advantages: (1) pseudo-halides Ac and BF₄ could form more stable Ac-Sn and BF₄-Sn bond, particularly at the grain boundaries to reduce Sn²⁺ oxidation; (2) the interaction of Ac⁻ (or BF₄⁻) with phenyl ring of PEA⁺ breaks the PEA+···PEA+ stacking, creating more uniformly distributed large organic cation PEA⁺ in the precursor solution; and (3) pseudo-halides Ac⁻ and BF₄⁻ can coordinate with Snl₂ in the precursor, allowing for greater control of nucleation and crystallization of quasi-2D tin perovskites and promoting both larger n-value quasi-2D tin perovskite phases and favorable vertically orientated quasi-2D phase grains. The films made by mixed PEAAc and PEABF₄ show narrow phase polydispersity, vertical orientation, superior stability, and oxidation resistance as compared with those made from PEAI. Taking these structural and chemical advantages, the quasi-2D tin perovskite films exhibit increased, balanced charge carrier mobility and reduced trap state density. A prominent efficiency of 8.9% is achieved for quasi-2D tin PSCs, which is among the highest efficiency of the reported state-of-the-art quasi-2D RP tin PSCs. Moreover, the quasi-2D tin PSCs retain 80% of the initial efficiency for 400 h in a N₂-filled glovebox without encapsulation. This work has opened a promising avenue to develop quasi-2D tin PSCs with high efficiency and stability.

RESULTS AND DISCUSSION

Preparation and characterization of thin films

The quasi-2D tin perovskite thin films with the formula $PEA_2FA_4Sn_5I_{16}$ were fabricated using a one-step spin coating plus anti-solvent method. To minimize Sn^{2+} oxidation, an excess 10 mol % SnI_2 was added in the precursor. Toluene was used as the anti-solvent during the spin coating process to control crystal growth. The $PEA_2FA_4Sn_5I_{16}$ perovskite thin films fabricated using PEA^+ with different anions were noted as PEAI, PEAAC, $PEABF_4$, and $PEAAC + PEABF_4$ ($Ac^-:BF_4^- = 7:3$), respectively.

To understand the effect of different anions in the precursor and subsequent crystal-lization process, we collected the attenuated total reflection Fourier transform infrared (ATR-FTIR) spectra of pure PEAI, PEAAc, and PEABF₄ powder and their mixtures with SnI₂, as shown in Figures 1A and 1B. The sp² C–H stretching of the phenyl ring in PEAI is located at 3,029 cm⁻¹ 45,46 attributed to the intermolecular interaction (PEA···PEA) of -CH on the side chain of PEA⁺ and π electrons on the phenyl ring of PEA⁺ as illustrated in Figure 2A. This peak almost disappeared for PEAAc and PEABF₄ (Figure 1A), indicating that the intermolecular CH··· π interaction between PEA···PEA in PEAI is largely replaced by the interaction between the phenyl ring of PEA⁺ and Ac⁻ or BF₄⁻ anion as illustrated in Figures 2B and 2C. Furthermore, when



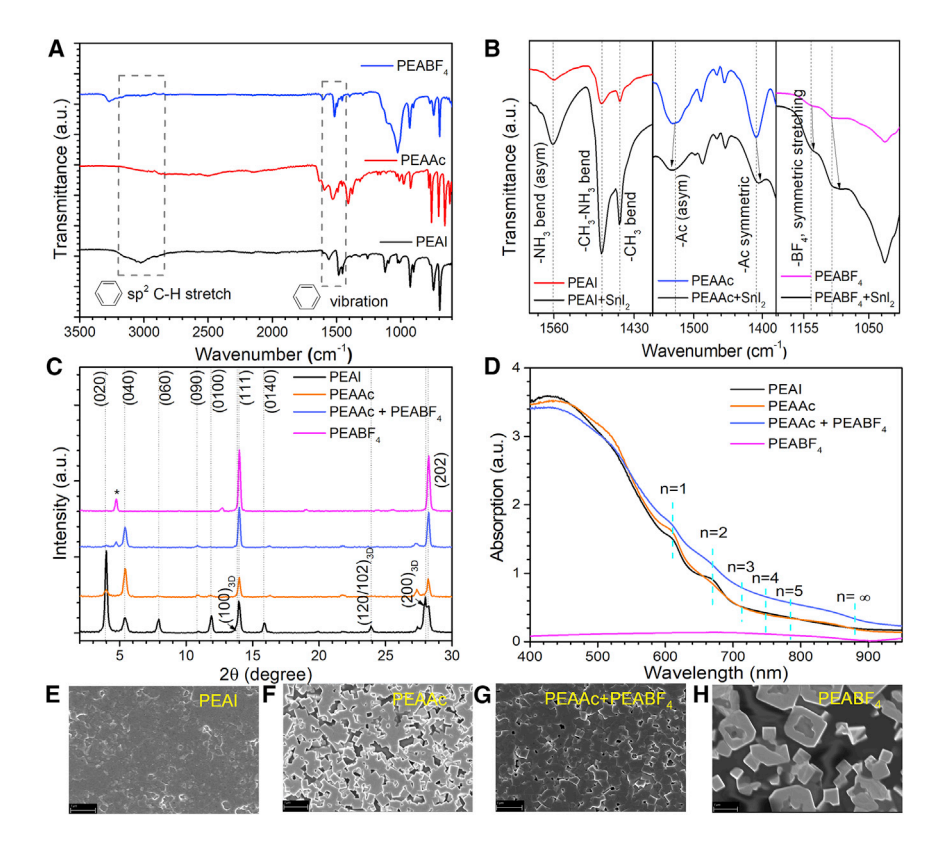


Figure 1. FTIR, XRD, UV-vis spectra, and SEM images of perovskite films

(A and B) Transmittance ATR-FTIR spectra: (A) powder of PEAI, PEAAc, and PEABF $_4$, and (B) PEAI and PEAI-SnI $_2$ mixture, PEAAc and PEAAc-SnI $_2$ mixture, and PEABF $_4$ and PEA BF $_4$ -SnI $_2$ mixture. (C) XRD patterns of quasi-2D PEA $_2$ FA $_4$ Sn $_5$ I $_1$ 6 perovskite films made from bulky organic cation (PEA $^+$) with different anions.

(D) UV-vis spectra of quasi-2D PEA $_2$ FA $_4$ Sn $_5$ I $_{16}$ perovskite films made from bulky organic cation (PEA $^+$) with different anions.

(E–H) Top-view SEM images of quasi-2D PEA $_2$ FA $_4$ Sn $_5$ I $_1$ 6 perovskite films made from bulky organic cation (PEA $^+$) with different anions. Quasi-2D PEA $_2$ FA $_4$ Sn $_5$ I $_1$ 6 perovskite films made from (E) PEAI, (F) PEAAc, (G) PEAAc+PEABF $_4$, and (H) PEABF $_4$. Scale bar, 1 μ m.

compared with PEAI, PEAAc, and PEABF₄ displayed completely distinct phenyl ring vibration peaks in the window of 1,400–1,700 cm⁻¹, indicating a different surrounding chemical environment for the phenyl ring of PEA. The coordination effect between pseudo-halides and SnI₂, as illustrated in Figures 2B and 2C, was confirmed by comparing the ATR-FTIR spectra of pure PEA⁺ salt powders with the mixture of PEA⁺ salt and SnI₂ (Figure 1B). For the mixed powder of PEAI and SnI₂, no peak shift was observed in comparison with pure PEAI powder, suggesting no interaction between PEAI and SnI₂.⁴⁷ The asymmetric and symmetric stretching vibrational peaks of the Ac⁻ group (-COO⁻) shifted from 1,530 to 1,533 cm⁻¹ and from 1,408 to 1,405 cm⁻¹, respectively, in pure PEAAc and upon the interaction of Ac⁻ with Sn²⁺ in the mixed powder of PEAAc and SnI₂.^{48,49} Similarly, the vibration peaks of BF₄⁻ in PEABF₄ shifted from 1,146, 1,107, and 1,024 cm⁻¹ to 1,140, 1,108, and 1,023 cm⁻¹, respectively, in the mixed powder of PEABF₄ and SnI₂, which could be induced by the interaction between BF₄⁻ and Sn²⁺.

Accordingly, Figures 2A–2C illustrate the crystallization process of $PEA_2FA_4Sn_5I_{16}$ perovskite thin films under different precursor conditions. The perovskite film fabricated by PEAI likely has a mixed 2D/3D BHJ structure with inhomogeneous

Article



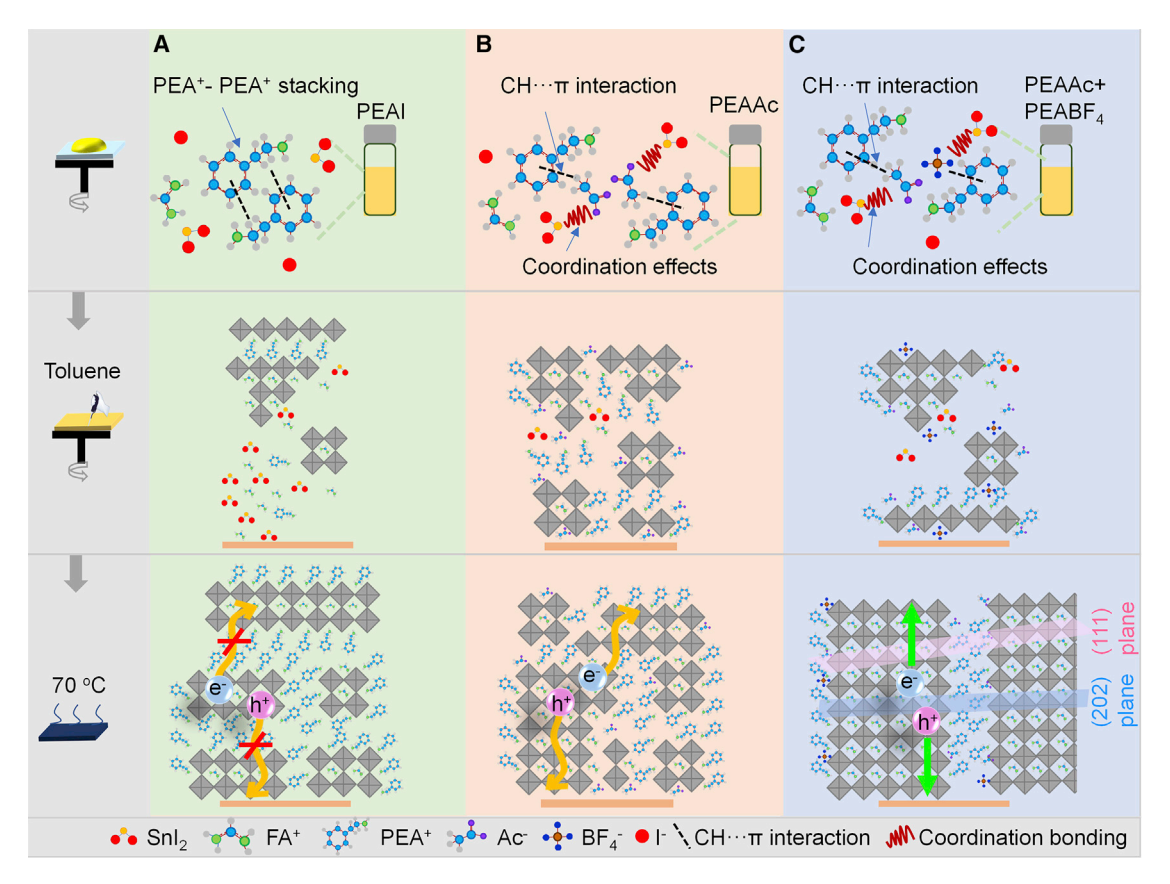


Figure 2. Schematics of the effect of pseudo-halide anions

(A–C) Schematics of the effect of pseudo-halide anions on the molecular interactions in the precursor solutions, nucleation, and initial growing process after adding toluene anti-solvent, and the possible final phase distribution in the quasi-2D tin perovskite thin films: (A) effect of PEAI, (B) effect of PEAAc, and (C) effect of PEAC + PEABF₄.

distribution because the PEA⁺···PEA⁺ stacking in the precursor causes local deficiencies of PEA⁺ for the growth of quasi-2D tin perovskites. As for the film prepared by PEAAc, Ac⁻ (CH₃COO⁻) anion forms sp³ CH $\cdots \pi$ interaction with the phenyl ring of PEA⁺ cation and -COO⁻···Sn²⁺ coordination with Snl₂. The interaction between pseudo-halide anions and the phenyl ring of PEA+ disrupts PEA...PEA stacking, potentially leading to a stable and homogeneous precursor solution. In addition, the strong coordination between pseudo-halide anions and Sn²⁺ could suppress Sn²⁺ oxidation and retard crystallization speed. Therefore, the perovskite thin films prepared by PEAAc could contain quasi-2D phases with reduced small n-value phases. While BF₄⁻ anion offers the same two effects as Ac⁻ anion, the stronger coordination between F⁻ and Sn²⁺ via the lone pair electron on F⁻ of BF₄⁻ could significantly slow the nucleation and crystallization processes. When adding both PEAAc and PEABF₄, the synergistic effects of Ac⁻ and BF₄⁻ anions could balance the growth rates of different phases and thus improve the phase purity and crystal orientation of the quasi-2D perovskite films. We conducted structural and spectroscopic studies to confirm the proposed possible crystal growth process and structures in the quasi-2D tin perovskite thin films prepared by using PEA salts with different anions.

X-ray diffraction (XRD) patterns were collected to investigate the influence of pseudo-halide anions on the structure of quasi-2D tin perovskite films (Figure 1C). Quasi-2D grains with parallel orientation to the substrate reveal all (0k0) planes (k



Cell Reports
Physical Science
Article

is an even integer), while those with perpendicular orientation to the substrate show predominantly (111) and (202) planes.²⁹ The presence of prominent (0k0) peaks in the PEAI quasi-2D tin perovskite thin film suggests preferential crystallization with (0k0) planes parallel to the film surface. The diffraction peaks of (020), (060), and (0100) planes are considerably smaller in the PEAAc perovskite film, indicating the reduction of small n-value quasi-2D tin perovskite phases. The PEAAc + PEABF₄ perovskite film exhibits a reduced intensity of (040) plane, indicating a reduced parallel orientation of quasi-2D phase due to the synergistic action of mixed pseudohalide anions. Furthermore, the dominant diffraction peaks at 14.0° and 28.2° ascribed to (111) and (202) planes of quasi-2D tin perovskites become more obvious and narrower full width at half-maximum (FWHM) in the PEAAc + PEABF₄ perovskite film, demonstrating that mixed Ac and BF₄ anions promote the out-of-plane growth of quasi-2D tin perovskite and increased crystallinity. For both PEAAc + PEABF₄ and PEABF₄ perovskite films, a new peak at $\theta = 4.7^{\circ}$ (*) appears. We suggest that this new XRD peak could be attributed to a 1D structure with edge-shared octahedra, where one or two I- anions are replaced by BF₄⁻ due to strong coordination between F⁻ and Sn²⁺ via the lone pair electrons on F⁻ of BF₄⁻. ^{50,51} This 1D tin perovskite could suppress tin oxidation and thus improve the stability of quasi-2D thin films and devices. 50,51

The ultraviolet-visible (UV-vis) absorption spectra of quasi-2D tin perovskite thin films are presented in Figure 1D. All tin perovskite films exhibit a similar absorption cut-off around 890 nm due to high n-value (n $\approx \infty$) quasi-2D phases or quasi-3D phase. The PEAI thin film exhibits two shoulder excitonic absorption peaks at 608 and 670 nm, which are attributed to n = 1 and 2 2D/quasi-2D tin perovskite phases, respectively. The peak at 670 nm (n = 2) diminishes in the PEAAc thin film and these two peaks nearly disappear in the PEAAc + PEABF₄ thin film, accompanied by an increase in overall absorption intensity in the 500–900 nm region. We attribute the disappearance of 608 and 670 nm peaks to the suppression of the small n-value (n = 1 and 2) 2D/quasi-2D tin perovskite phases in the thin film. The increased overall UV-vis intensity of the PEAAc + PEABF₄ film confirms the improved crystallinity, which is consistent with the XRD result. It is worth mentioning that the absorption intensity of the PEABF₄ film is substantially reduced, which is attributed to poor morphology and inadequate surface coverage.

Figures 1E–1H show the top-view scanning electron microscopic (SEM) images of PEAI, PEAAc, PEAAc + PEABF4, and PEABF4 thin films, respectively. The PEAI thin film has a typical densely packed polycrystalline microstructure with irregular grain boundaries. The PEAAc thin film shows flake-like grains with straight edges and sharp corner but more pin holes, leading to potentially increased recombination centers and leakage currents. The PEAAc + PEABF4 thin film resembles the surface morphology of the PEAAc film, but with less pin holes. The PEABF4 thin film forms large, dispersed grains, which indicates poor morphology and inadequate surface coverage. The large grain size of the PEABF4 thin film suggests that BF4 $^-$ can slow down the nucleation and crystal growth of 2D/quasi-2D phases. The synergetic effect of Ac $^-$ and BF4 $^-$ anions improves the morphology of the PEAAc + PEABF4 thin film. The XRD, UV-vis, and SEM results provide partial evidence for the anion effects on the quasi-2D tin thin-film formation processes proposed in Figure 2.

To further elucidate the crystal structure of tin perovskite thin films fabricated with PEA $^+$ paired with different anions, grazing-incidence wide-angle X-ray scattering (GIWAXS) measurements were performed with the incident angle varying from 0.05° to 0.25° to track the structural profiles from surface to bulk of thin films

Article



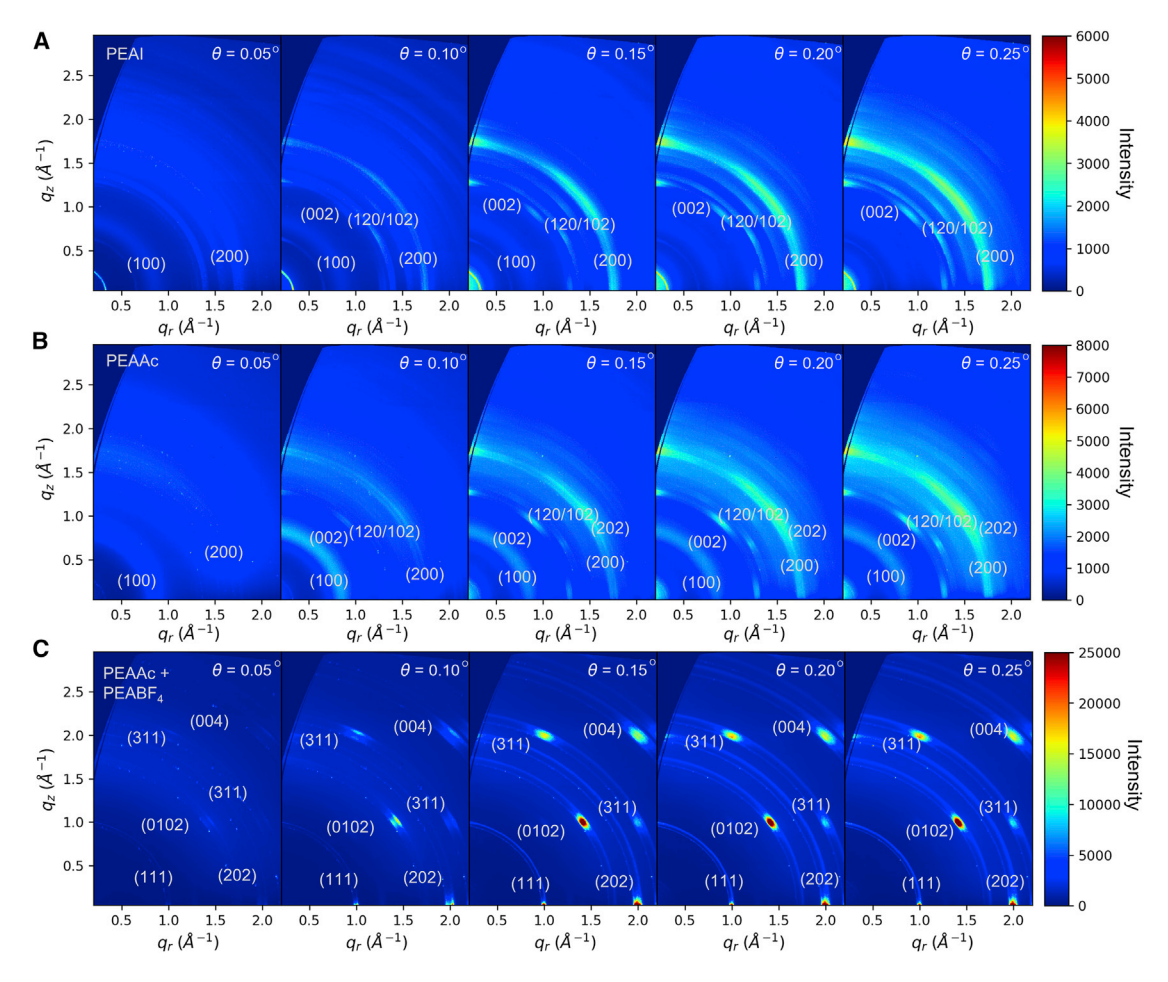


Figure 3. GIWAXS patterns of quasi-2D Sn perovskite films

- (A) GIWAXS pattern of PEAI perovskite film with incident angles θ = 0.05° to θ = 0.25°.
- (B) GIWAXS pattern of PEAAc perovskite film with incident angles $\theta = 0.05^{\circ}$ to $\theta = 0.25^{\circ}$.
- (C) GIWAXS pattern of PEAAc + PEABF₄ perovskite film with incident angles $\theta = 0.05^{\circ}$ to $\theta = 0.25^{\circ}$.

(Figures 3A–3C). ¹⁹ A high-energy beam (13.4 keV) was used in our GIWAXS experiments to reach the bottom of our thin films (~300 nm, Figure S1) with the incident angle of 0.25°. In the PEAI thin film, as the incident angle increases from 0.05° to 0.25°, three Debye-Scherrer rings associated with (100), (120/102), and (200) planes emerge (Figure 3A), indicating the existence of 3D perovskite grains with random orientation in the film. The (002) Bragg spot (Figure 3A) ascribed to a small n-value 2D/quasi-2D phase, which appears alongside the aforementioned 3D perovskite planes, indicates a mixed 2D/3D structure in the PEAI thin film. The PEAAc thin film exhibits the similar GIWAXS patterns of the PEAI thin film, except higher intensity and the emergence of the rings corresponding to (202) and (100) planes at large incident angles (Figure 3B). We infer that the PEAAc perovskite film has improved crystallinity with a mixed 2D/3D structure and more quasi-2D phases at the bottom. For the PEAAC + PEABF₄ thin film (Figure 3C), sharp and discrete Bragg spots under all the incident angles were observed, indicating the formation of low-dimensional polycrystalline with preferential orientation uniformly distributed throughout the film. In particular, the crystal domains are orientated with their (111) and (202) planes parallel to the substrate surface, indicating out-of-plane growth as illustrated in Figure 2C, which is favorable for the charge transfer process. It is also obvious that small



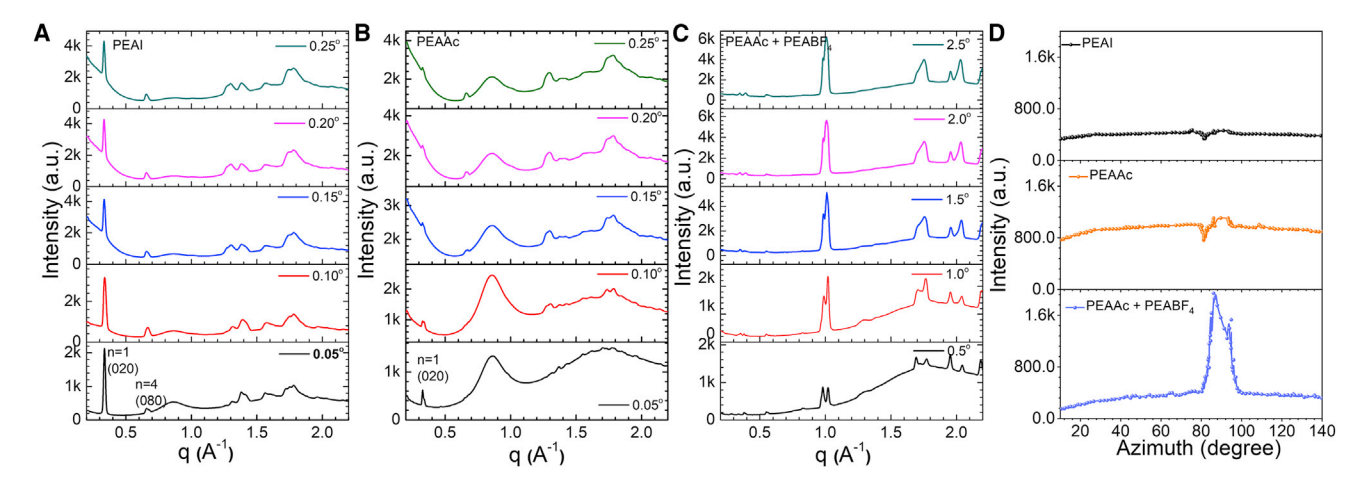


Figure 4. GIWAXS line-cut profiles of quasi-2D Sn perovskite films

(A-C) Intensity versus q plots for the diffraction features of quasi-2D Sn perovskite films along with the evolution of the incident angle from 0.05° to 0.25°:

(A) PEAI perovskite film, (B) PEAAc perovskite film, and (C) PEAAc + PEABF₄ perovskite film.

(D) Pole figures of the azimuth angle of quasi-2D Sn perovskite films at $q = 1 \text{ Å}^{-1}$, the (111) plane.

n-value phases (q_r , $q_z < 0.5 \text{ Å}^{-1}$) are reduced for the PEAAc perovskite film and nearly disappear for the PEAAc + PEABF₄ perovskite film. To elucidate the synergetic effect of Ac⁻ and BF₄⁻ anions, we varied the ratio of Ac⁻:BF₄⁻: the GIWAXS patterns clearly show the features of Debye-Scherrer rings in the films with the ratios of Ac^- : BF₄ of 9:1 and 8:2 and the features of Bragg spots in the films with the ratios of 7:3, 6:4, and 5:5 (Figure S2). Using PEABF₄ only, the GIWAXS patterns of the PEABF₄ film exhibit no Bragg spots but Debye-Scherrer rings corresponding to (111), (202), (0102), and (311) planes of quais-2D phases (Figures S2 and S3). These results further support the possible mechanisms we proposed in Figure 2. While Acanions suppress the growth of quasi-3D phase and low n-value quasi-2D phases by breaking PEA⁺···PEA⁺ stacking and making -COO⁻···Sn²⁺ coordination, BF₄⁻ anions offer similar but even stronger effects, which negatively impact the formation of high-quality quasi-2D thin films. However, mixing Ac⁻ and BF₄⁻ anions in an appropriate range (e.g., BF_4^- 30%–50%), the synergetic effect not only promotes large n-value (mainly n = 3-5) quasi-2D phases but also out-of-plane oriented quasi-2D grains.

Figures 4A-4C compare the corresponding intensity versus q (where q is the scattering vector (q = $4\pi \sin(\theta)/\lambda$) for the diffraction features) for different guasi-2D tin perovskite films. The scattering peak at $q = 1 \text{ Å}^{-1}$ corresponds to the (111) plane of quasi-2D PEA₂FA₄Sn₅I₁₆ perovskite, while $q = 0.33 \text{ Å}^{-1}$ and $q = 0.65 \text{ Å}^{-1}$ correspond to the (020) plane of n = 1 phase and the (080) plane of n = 4 phase, respectively. The scattering peak intensity at q = 0.33 $\mbox{\normalfont\AA}^{-1}$ becomes less obvious for the PEAAc and PEAAc + PEABF₄ films compared with the PEAI film, indicating a reduced n = 1 analog in the films by using pseudo-halide anions. A strong (111) plane scattering peak appears in the PEAAc + PEABF₄ film, indicating that BF₄⁻ anion is beneficial for the formation of well-aligned quasi-2D tin perovskite octahedral slabs as illustrated in Figure 2C. Compared with the PEAAc + PEABF₄ perovskite film, the PEAI and PEAAc perovskite films show that intense, but broad peaks span over wider polar angles at low q values. It is more likely that small n-value (n < 5) phases exist with mixed 2D/3D structures, which is incontrovertibly brought about by the weaker Sn-I bonding. Clearly, using Ac anion combined with BF₄ anion is more favorable for forming the (111) plane of quasi-2D Sn perovskite thin films. The crystal

Article



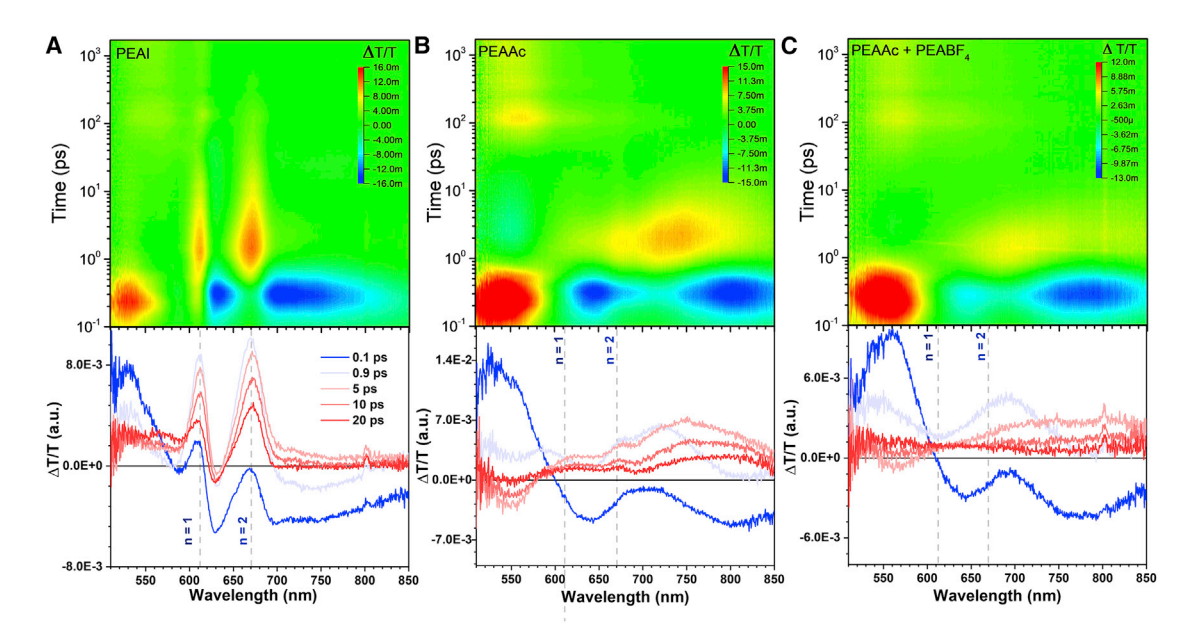


Figure 5. TA spectrum of quasi-2D Sn perovskite films (A–C) The pseudo-color (Δ T/T) TA plots (upper panel) and TA spectra at various delay times (lower panel) of quasi-2D Sn perovskite films excited by a 3.02 eV (410 nm) photon pulse with an initial carrier density n_0 of 1.2 × 10^{16} cm⁻³: (A) PEAI perovskite film, (B) PEAAc perovskite film, and (C) PEAAc + PEABF₄ perovskite film.

orientation with respective to the substrate was further analyzed. The pole figures of the Azimuth angle at $q=1\ \mathring{A}^{-1}$, i.e., the (111) plane, are presented in Figure 4D with the same y scale. The PEAI perovskite film shows no obvious arcs indicating no preferential orientations. The increased arc intensity around 90° exhibited by the PEAAc perovskite film suggests a weak preferential orientation of quasi-2D grains. The strong arc intensity around 90° exhibited by the PEAAc + PEABF4 perovskite film indicates a highly vertical orientation of quasi-2D grains. The GIWAXS studies further support the proposed crystal growth processes as illustrated in Figure 2C when the mixed pseudo-halide anions are used. The 2D inorganic slabs in the PEAAc + PEABF4 perovskite film are perpendicular with respect to the substrate, producing continuous, vertical charge-transport channels, which facilitates high performance PSCs.

Phase distribution and charge carrier dynamics

To gain a deeper understanding of phase distribution and charge carrier dynamics in quasi-2D tin perovskite films, femtosecond transient absorption (TA) spectroscopic measurements were conducted. All films were excited from the perovskite film side under a 3.02 eV (410 nm) photon pulse. The obtained TA spectra in pseudo-color plots and at various delay times are shown in Figures 5A–5C and S4. Hot charge carriers were generated simultaneously in the high energy states of the conduction bands for all phases (n = 1, 2, 3, 4, 5, and ∞). These hot carriers subsequently cool to the band edge states or transfer their energy to the adjacent quasi-2D phases. The positive photoinduced changes in transmission (Δ T/T) (i.e., photobleaching) indicate state filling of specific optical transitions. The cooling of hot charge carriers to their band edge states induces a photobleaching process associated with these states. This band edge exciton transition associated with different n-value 2D/quasi 2D phases inside the film can be recognized at the early probe delay time. Second 10 and 670 nm can be ascribed to n = 1 and



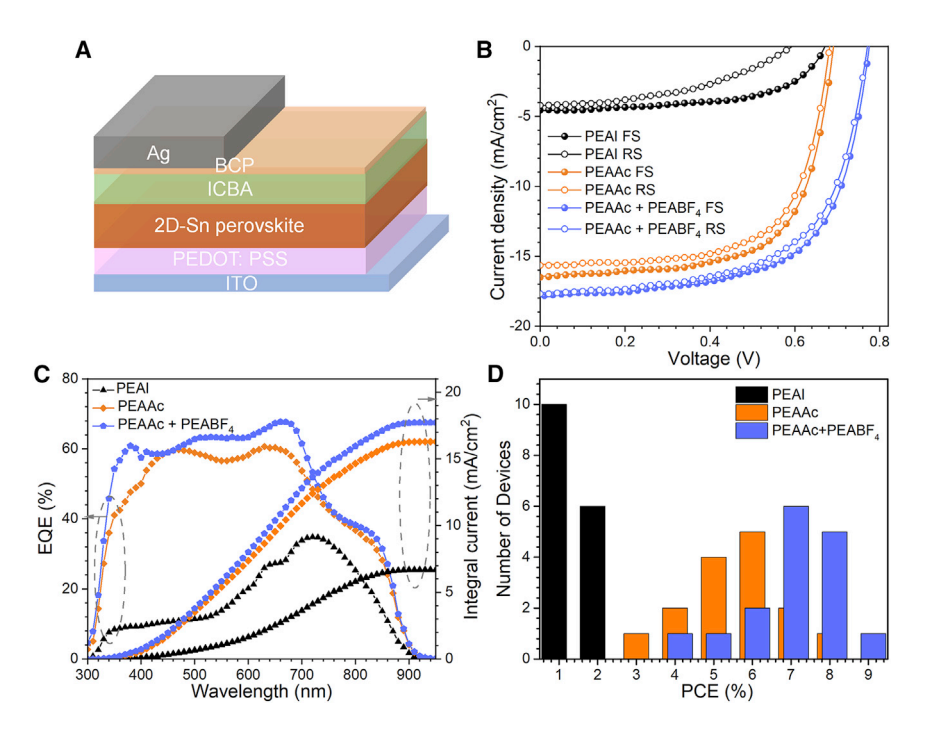


Figure 6. Device structure illustration, performance, band position, and light-intensitydependent measurements

- (A) Schematic illustration of quasi-2D tin PSCs.
- (B) J-V curves of the PSCs with PEAI, PEAAc, and PEAAc + PEABF₄ quasi-2D tin perovskite films.
- (C) Corresponding EQE spectra of the PSCs with PEAI, PEAAc, and PEAAc + PEABF $_4$ quasi-2D tin perovskite films.
- (D) PCE histogram of the PSCs with PEAI, PEAAc, and PEAAc + PEABF $_4$ quasi-2D tin perovskite films.

n = 2 2D/quasi 2D perovskite phase, respectively. ¹⁹ The decay of these peaks takes about 100 ps, indicating an inefficient charge transfer, presumably due to the grains of these small n-value phases embedded in 3D phase grains.⁵⁴ In contrast, the PEAAc film exhibits nonobvious photobleaching peaks associated with undesired small n-value 2D/quasi 2D phases at the very early delay time (<0.9 ps) (Figure 5B). A broader peak in the range of ~670-800 nm, corresponding to multiple high n-value phases, decays quickly (\sim 10 ps), indicating faster charge transfer benefiting from the elimination of small n-value 2D/quasi-2D phases. Furthermore, using a mixture of PEAAc and PEABF4 leads to the film with a total suppression of photobleaching peaks associated with small n-value 2D/quasi 2D phases but a narrower peak ranging ~670-750 nm (Figure 5C), indicating a narrower phase distribution. These phenomena reveal that small n-value (n = 1 and n = 2) 2D/quasi 2D phases are reduced in the PEAAc film and nearly eliminated in the PEAAc + PEABF₄ film, which is consistent with the UV-vis, XRD, and GIWAXS results. A monodispersing of 2D perovskite phases corresponds to a small spread of band gaps of absorbers, indicating reduced traps in the film. In this regard, the PEAAc + PEABF4 film with reduced small n-value phases will have a smoother charge transfer route compared with PEAI and PEAAc films. 53,54

Fabrication and analysis of PSCs

We made PSCs by deploying aforementioned quasi-2D tin perovskite films in the structure of ITO/PEDOT:PSS (40 nm)/quasi-2D tin perovskite (300 nm)/ICBA (60 nm)/BCP (10 nm)/Ag (100 nm) (Figure 6A). We have varied the ratio of PEAAc

Article



Table 1. Average photovoltaic parameters and the best performance device photovoltaic parameters in parentheses of PSCs with different active layers

Device	V _{OC} (V)	J_{SC} (mA/cm ²)	FF	PCE (%)
PEAI	0.62 ± 0.03 (0.67)	4.3 ± 0.49 (4.6)	0.53 ± 0.03 (0.57)	1.41 ± 0.22 (1.8)
PEAAc	$0.66 \pm 0.02 (0.69)$	16.1 ± 0.43 (16.5)	$0.64 \pm 0.02 (0.66)$	$6.79 \pm 0.44 (7.5)$
PEAAc + PEABF ₄	0.76 ± 0.01 (0.78)	17.2 ± 0.48 (17.8)	0.62 ± 0.02 (0.64)	8.11 ± 0.40 (8.9)

and PEABF₄. The device performance parameters and external quantum efficiency (EQE) spectra are summarized in Figure S5, showing the best performance devices containing the PEAAc + PEABF₄ quasi-2D tin perovskite film, i.e., PEAAc:PEABF₄ = 7:3. As shown in Figure 6B, the PSC containing the PEAAc + PEABF₄ perovskite film shows the highest performance up to 8.9% under standard AM1.5G illumination (1 sun), with V_{OC} of 0.78 V, short-circuit current density (J_{SC}) of 17.8 mA/cm², and fill factor (FF) of 64.1%, whereas the PEAAc perovskite film-based device exhibits an efficiency of 7.5% with V_{OC} of 0.69 V, J_{SC} of 16.5 mA/cm², and FF of 66.1%, and the PEAI perovskite film-based device exhibits an efficiency of 1.8% with V_{OC} of 0.67 V, J_{SC} of 4.6 mA/cm², and FF of 66.1%. Table 1 summarizes the average and the best performance device photovoltaic parameters. The significant improvements of J_{SC} and V_{OC} exhibited by the PEAAc and PEAAc + PEABF₄ PSCs may be attributed to the vertically orientated 2D grains and the reduced small n-value guasi-2D phases, which lead to reduced charge carrier recombination and improved charge carrier transport, even though some pinholes are shown in these films (Figures 1F and 1G). It is worth mentioning that the PEAAc + PEABF₄ PSC exhibits an ignorable hysteresis in comparison with the PEAI and PEAAc PSCs (Figure 6B), which reflects the low trap state density and reduced interface charge accumulation in the device. The EQE spectra of the PEAAc and PEAAc + PEABF4 PSCs show an improved charge collection efficiency in the full scope (Figure 6C). Note that the EQE of the PEAAc + PEABF₄ PSC shows further enhanced efficiency in the spectral range of 300-400 and 500-700 nm compared with the PEAAc PSC, which are contributed by the reduced small n-value quasi-2D phases and increased film crystallinity. The integrated currents from the EQE measurements closely match the J_{SC} values from the J-V curves. Figure 6D shows the efficiency distribution of the devices containing different active layers. In comparison with the PEAI perovskite film-based devices, both the PEAAc and the PEAAc + PEABF₄ perovskite film-based devices show statistically significant higher PCEs, demonstrating superior reproducibility.

To investigate whether the mixture of Ac^- and I^- and the mixture of BF_4^- and I^- can also improve the performance of quasi-2D tin PSCs, we fabricated devices with the thin films made by varying the ratios of PEAI:PEAAc and PEAI:PEABF₄ as 10:0, 7:3, 5:5, 3:7, and 0:10 for each pair. The forward and backward scan J-V curves and the statistical representation of the photovoltaic parameters of these PSCs are presented in Figures S6-S8. The devices made by PEAAc + PEAI show descent J-V curves and reduced hysteresis with the increase of PEAAc (Figure S7A). Poor J-V curves with large hysteresis are observed for the devices made by PEABF₄ + PEAI (Figure S6B). Compared with the device made by pure PEAI with an average PCE of \sim 1.5%, the PCE increases monolithically with the increase of PEAAc content to \sim 6.8%, mainly due to the significant increase of J_{SC} and slightly increased FF and V_{OC} (Figure S7). The opposite trend is observed with the increasing of PEABF₄, which is mainly due to the decrease of V_{OC} (Figure S8). The full sets of PEAI + PEABF₄ devices exhibit very low PCEs (\sim 0.1% to \sim 1.5%). This could be attributed to the poor thin-film coverage and low absorption caused by large scattering of large, uneven particles in the films as shown in Figures 1D and 1H.

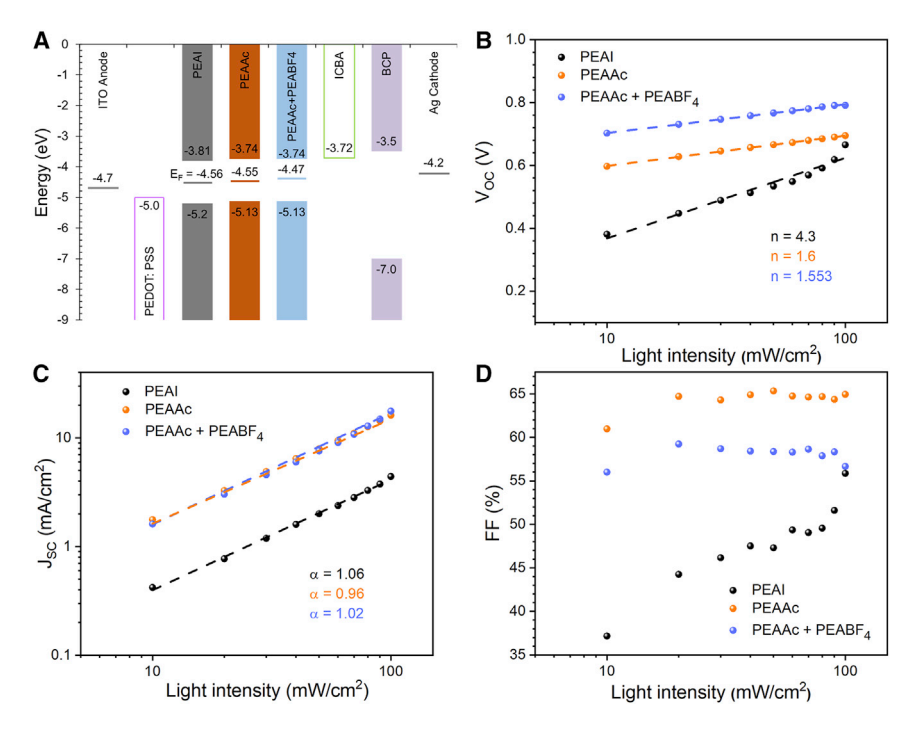


Figure 7. Band position and light-intensity-dependent measurements

(A) The energy level alignment of quasi-2D tin perovskite devices containing the PEAI, PEAAc, and PEAAc + PEABF₄ active layers.

(B–D) Light intensity dependence of J-V characteristics of the quasi-2D tin device parameters: (B) open-circuit voltage (V_{OC}), (C) short-circuit current density (J_{SC}), and (D) fill factor (FF).

The valence band maximum and Fermi level (E_F) of different quasi-2D tin perovskite thin films were characterized by UV photoemission spectroscopy (UPS) (Figure S9). Figure 7A shows that the PEAAc and PEAAc + PEABF₄ perovskite films show an upward shift of the band position, which might result in reduced energy losses and contribute to the increased V_{OC} of the PSCs. Furthermore, the E_F of the PEAAc and PEAAc + PEABF₄ perovskite films are more toward neutral semiconductors than the PEAI perovskite film. The neutral Fermi level differs from the 3D tin perovskites that exhibit p-type nature due to Sn^{4+} self-doping. This phenomenon indicates that the Sn^{2+} oxidation process has been effectively suppressed by adopting quasi-2D tin perovskites and using pseudo-halide anions.

Trap state density and charge carrier mobility of different quasi-2D tin perovskite films have direct impact on the device performance. Therefore, we fabricated electron-only and hole-only devices as shown in the insets of Figures S10A and 10B, respectively. The electron and hole trap state density, N_{trap} , was extracted by fitting the log-scale dark *J-V* curves (Figures S10A and 10B) to the space charge-limited current model: 55

$$N_{trap} = \frac{2\varepsilon_0 \varepsilon_r V_{TFL}}{qL^2},$$
 (Equation 1)

where L is the thickness of the quasi-2D tin perovskite thin film, ε_r is the relative dielectric constant, ε_0 is the vacuum permittivity, q is the elemental charge, and V_{TFL} is the onset voltage of the trap-filled limit region. The relative dielectric constant for halide perovskite is around 25. The electron and hole trap densities are summarized in Table S1. In comparison with the PEAI perovskite film, the PEAAc and PEAAc + PEABF₄ perovskite films have a slightly lower electron trap density but

Article



hole trap density is reduced about half, particularly in the PEAAc + PEABF₄ perovskite film, which is ascribed to the reduction of $\rm Sn^{2+}$ oxidation by pseudo-halides. ⁵⁷ In addition, the intrinsic electron and hole mobility, μ , was estimated by fitting the dark *J-V* curves using the Mott-Gurney law: ⁵⁵

$$J_D = \frac{9\varepsilon\varepsilon_0 \mu V_b^2}{8I^3},$$
 (Equation 2)

where V_b and J_D are applied voltage and dark current, respectively. Both electron and hole mobility are increased in the PEAAc and PEAAc + PEABF₄ perovskite films compared with the PEAI film (Table S1). The more balanced electron and hole charge transport exhibited by the PEAAc + PEABF₄ perovskite film tends to reduce the charge acclamation at the interfaces of the hole and electron transport layers and the perovskite layer. These superior charge transport properties are mainly attributed to the low trap density resulting from the reduced Sn^{2+} oxidation, providing a higher chance for achieving longer carrier lifetime and collection efficiency.

To further understand charge recombination mechanisms in PSCs with different quasi-2D perovskite films, we measured the J-V curves of the PSCs illuminated with the light intensity varied from 100 mW/cm² (1 Sun) to 10 mW/cm² (0.1 Sun) (Figure S11) and investigated the evolution of V_{OC} , J_{SC} , and FF as a function of light intensity. The V_{OC} shows a logarithmic dependence on light intensity with a slope of nkT/q, where n represents different recombination mechanisms, k_B is the Boltzmann constant, T is the absolute temperature, and q is the elementary charge. When n > 2, monomolecular recombination dominates and trap states play a significant role, while when n \sim 1, bimolecular recombination dominates, demonstrating minimal shallow trap states in the perovskites.⁵⁸ Figure 7B shows the slope of the PEAI PSC is 4.3, whereas the slopes of the PEAAc and the PEAAc + PEABF₄ PSCs are 1.60 and 1.55, respectively, indicating that the monomolecular, trap-state-assisted recombination is more prevalent in the PEAI PSC, whereas bimolecular, free carrier recombination dominates in the PEAAc and PEAAc + PEABF₄ PSCs. In particular, the slope of the PEAI PSC is away from linear close to one solar illumination, suggesting that a significant amount of trap-state-assisted recombination occurs at the interfaces due to poor charge transport properties and surface charge accumulation. The power law dependence of J_{SC} on light intensity ($J \propto I^{\alpha}$) is shown in Figure 7C, in which the double logarithmic scale of J_{SC} and light intensity are plotted. The solar cell with carrier imbalance or an interfacial barrier shows a space charge limited behavior having a power law relationship with $\alpha = 3/4$, while a device with no space charge effects shows an α value close to 1. Compared with the PEAI and PEAAc PSCs, the PEAAc + PEABF₄ PSC shows an α value closest to 1, indicating the weakest space charge effect. These results are consistent with the reduced hole trap state density and increased, balanced hole and electron mobility in the PEAAc + PEABF₄ film revealed by charge transport study using hole- and electron-only devices. The FF as a function of logarithmic scale light intensity is shown in Figure 7D. The change in FF with respect to change in light intensity has been attributed to the series resistance, shunt resistance, and bimolecular recombination. ^{59,60} The series resistance and shunt resistance related to the perovskite film quality, while the bimolecular recombination process here is mostly affected by the oxidization of Sn²⁺. The FF of the PEAI PSC drops dramatically in the low light intensity region, whereas the FF of the PEAAc and PEAAc + PEABF₄ PSCs remain static. This implies that highquality perovskite films have been fabricated in the PEAAc and PEAAc + PEABF4 based devices. The reduced recombination and high-quality perovskite film play an important role in the super high charge collection ability and excellent device performance.



Cell Reports
Physical Science
Article

To evaluate the effect of pseudo-halide anion engineering on the film and device stability of quasi-2D tin perovskites, we collected the UV-vis absorption spectra of different quasi-2D tin perovskite films with the evolution of time (Figure S12) and performed the aging tests on the best-performance PSCs that were kept under dark in a N2-filled glovebox without any encapsulation. The PEAI perovskite film shows a noticeable decrease of absorption after 30 min (Figure S12A) while the PEAAc film delays to ~90 min (Figure S12B). The PEAAc + PEABF₄ film shows ignorable absorption reduction below 700 nm and slightly reduced absorption in the 700-900 nm range up to 120 min of the testing time (Figure S12C), which proves the stable quasi-2D phases in the film. The improved film stability is attributed to the strong interaction between Ac⁻, or BF₄⁻ anion and Sn²⁺, which significantly reduces the oxidation of unbonded Sn²⁺. Also, the improved stability by pseudo-halide anion engineering suspects the reduced Sn⁴⁺ inside the film, which is one of the key factors that promote the higher V_{OC} of the devices. Figure \$13 shows that the PEAAc + PEABF₄-, PEAAc-, and PEAI-based tin PSCs retained \sim 80% of their initial efficiency up to 400, 300, and 40 h, respectively. Notably, the major reduction of the stability comes from the loss of V_{OC} for the PEAI-based PSC (Figure S13B), which is a key indicator of the oxidization of Sn²⁺ inside the perovskite film. It should be pointed out that we only added 10 mol % Snl₂, not commonly used additives, such as SnF₂, in making tin perovskite thin film with the intention to suppress Sn²⁺ oxidation while avoiding phase segregation. In addition, we made the precursor with the molar ratio of each component to the target chemical formula for < n > =5 RP tin phase. We adopted the inverted device architecture with PEDOT:PSS and ICBA as the hole and electron transport layers, respectively. All these factors could result in lower performance and shorter lifetime of our control PEAI devices compared with those reported in literature. 61,62 It is worth noting that the 8.9% efficiency is among the highest PCE in the reported state-of-the-art of quasi-2D Snbased PSCs and comparable with to the mixed 2D/3D or pure 3D Sn PSCs (Table S2).

In this work, we explored the use of a large organic cation (PEA⁺) paired with pseudo-halide anions (Ac⁻ and/or BF₄⁻) to make quasi-2D RP perovskites with a formula of PEA₂FA₄Sn₅I₁₆. The Ac⁻ and BF₄⁻ pseudo-halide anions can not only break the PEA+...PEA+ stacking that exists in PEAI but also coordinate with Sn²⁺ ions. The dual-effect results in uniformly distributed PEA⁺ in the precursors and reduced small n-value phases in the quasi-2D tin perovskite films. The synergistic effect by using mixed PEAAc and PEABF4 leads to the quasi-2D tin perovskite film with increased crystallinity, preferred orientation, decreased trap state density, and increased, balanced electron and hole mobility. The suppressed Sn²⁺ oxidation due to the surface passivation by pseudo-halide anions enables a better film stability. As a result, a record high efficiency of 8.9% is achieved for quasi-2D $PEA_2FA_4Sn_5I_{16}$ PSCs. The device based on $PEAAc + PEABF_4$ film shows much enhanced stability and retains 80% of its initial PCE for 400 h in the N2 environment without encapsulation. This work sheds light on the role of pseudo-halide anions in making quasi-2D tin perovskites with desired phase and orientation, and provides an effective way to develop quasi-2D tin PSCs with high efficiency and stability.

EXPERIMENTAL PROCEDURES

Resource availability

Lead contact

Further information and requests for resources and reagents should be directed to and will be fulfilled by the lead contact, Qiuming Yu (qy10@cornell.edu).

Cell Reports Physical Science

Article



Materials availability

This study did not generate new unique materials.

Data and code availability

This study did not generate datasets.

Chemical materials

Tin (II) iodide (SnI₂) (99.99%), phenylethylamine (PEA) (99%), acetic acid (HAc) (99%, aqueous solution), tetrafluoroboric acid solution (HBF₄) (48 wt % in H₂O), N,N-dimethylformamide (DMF) (anhydrous, \geq 99.8%), diethyl ether (\geq 99%), chlorobenzene (anhydrous, 99.8%), N,N-dimethyl sulfoxide (DMSO) (anhydrous, \geq 99.9%), ethanol (\geq 99.5%), isopropanol, and bathocuproine (BCP) (99.99%) were purchased from Sigma-Aldrich (St. Louis, MO) without further purification. Formamidinium iodide (FAI) and phenethylammonium iodide (PEAI) were purchased from GreatCell Solar (Queanbeyan, Australia) without further purification. Di[1,4]methanonaphthaleno [1,2:2',3';56,60:2",3"][5,6]fullerene-C60-lh, 1',1",4',4"-tetrahydro (ICBA) (99.9%) was purchased from 1-Material (QC, Canada).

PEAAc and PEABF₄ synthesis

PEAAc was synthesized by dissolving phenylethylamine (10 mL, 80 mmol) in 10 mL of ethanol in an ice bath. Acetic acid aqueous solution (9.73 mL, 170 mmol) was added dropwise to the flask with vigorous stirring. After the addition of acetic acid, the mixture was allowed to stand in an ice bath for another 20 min until a colorless precipitate appeared. The precipitate was filtered under vacuum and washed thoroughly using cold diethyl ether. The crude precipitate was collected and recrystallized in ethanol twice to obtain thin, plate-like white crystals. PEABF₄ was synthesized following the same procedure but simply replacing acetic acid aqueous solution to HBF₄ aqueous solution (22 mL, 170 mmol).

2D tin perovskite thin-film fabrication

Plain glass substrates (Thermo Fisher Scientific) were cut into 15 × 15 mm size pieces and cleaned via ultrasonication for 15 min in detergent in Millipore deionized water, Millipore deionized water, acetone, and isopropanol in sequence. The cleaned substrates were treated with oxygen plasma at 100 W for 10 min. The substrates were transferred to a N₂-filled glovebox to make 2D tin perovskite films. For PEAI-based perovskite thin film, a 0.16 M perovskite PEA₂FA₄Sn₅l₁₆ precursor composed of PEAI (0.32 mM), FAI (0.64 mM), and Snl₂ (0.88 mM) (10 mol % excess Snl₂) were added in a 1 mL mixed solvent (DMF:DMSO = 3:1) and stirred at 70°C for 1–2 h. Perovskite films of PEAAc or PEAAc + PEABF₄ with different ratios were made by changing PEAI to PEAAc or PEAAc + PEABF₄ and kept PEA⁺ cation at 0.32 mM. The precursor was filtered with a 0.22 µm PTFE filter before spin coating. A 2D tin perovskite film was fabricated by spin coating a 30 µL precursor solution at 1,000 and 5,000 rpm for 10 and 25 s, respectively. Toluene (800 µL) was dropped during the second spin process at 20 s before the end of the second spin step. The substrate was annealed at 70°C for 10 min.

Film characterization

SEM images were acquired using an FEI Sirion SEM operated at 3 kV to analyze the surface morphology. 2D XRD patterns were collected with a Bruker GADDS D8 Focus Powder Discover diffractometer using Cu K α radiation (λ = 1.5419 Å) and the data were processed using the EVA package provided by Bruker AXS to investigate the crystal structures of perovskite thin films. UV-vis absorption spectra were collected using a Varian Cary 5000 UV-vis-NIR spectrophotometer. FTIR were



Cell Reports
Physical Science
Article

collected using a Bruker Vertex V80V coupled with an ATR accessory (MIRacle ATR, PIKE Technologies).

UPS measurements were conducted using a Scienta Omicron ESCA-2SR with operating pressure ca. 1 × 10^{-9} Torr. Monochromatic Al K α X-rays (1,486.6 eV) were generated at 250 W (15 kV; 20 mA) with photoelectrons collected from a 2 mm diameter analysis spot. Photoelectrons were collected at a 0° emission angle with source to analyzer angle of 54.7°. A hemispherical analyzer determined electron kinetic energy, using a pass energy of 200 eV for wide/survey scans, and 50 eV for high-resolution scans. A flood gun was used for charge neutralization of non-conductive samples.

The grazing-incidence wide-angle X-ray scattering (GIWAXS) measurements were conducted at the Complex Materials Scattering (CMS) (11-BM) beamline of the National Synchrotron Light Source II at Brookhaven National Laboratory. The X-ray beam has a size of 200 μm (horizontally) \times 50 μm (vertically), divergence of 1 mrad, and energy of 13.5 keV with a resolution of 0.7%. The perovskite films were deposited on ITO glass 1.5 x 1.5 cm, and three positions were measured with an exposure time of 10 s at incident angles of 0.05°, 0.1°, 0.15°, 0.2°, and 0.25° with respect to the substrate plane. The penetration depth can be calculated by: $\frac{1}{A(\alpha_i)} = -2k_0 Im[\sqrt{\alpha_i^2 - \alpha_c^2 - 2i\beta}]$, where $k_0 = 2\pi/\lambda$ is the elastically conserved wave vector modulus and λ is X-ray wavelength, α_i is the incidence angle, α_c is the critical angle for total external reflection, and β is related to the linear absorption coefficient of intensity, μ , through $\beta = \lambda * \mu/(4*\pi)$. The scattered data were collected with a customized Pilatus 800K area detector (Dectris, Switzerland), which consists of 0.172 mm square pixels in a 1,043 \times 981 array, placed \sim 0.260 m downstream of the sample position. The collected 2D scattering patterns were analyzed by a Python package provided by the beamline staff.

Broadband pump-probe TA spectroscopy measurements were performed on a Helios Fire spectrometer (Ultrafast Systems) using a fs-pulsed Pharos (1 mJ)/Orpheus/Lyra Light Conversion system as regenerative amplifier/optical parametric oscillator/frequency doubler system for generating the probe and the pump lights at a repetition rate of 1 kHz. Pump light (400 nm) was generated in an Orpheus/Lyra system depolarized prior to the sample while the white light was generated using a percentage of the fundamental beam (1,030 nm) focused on a Sapphire crystal. An optical delay placed in the probe beam path provided a dynamic range up to 7 ns and an overall temporal resolution down to the pulse width of the laser (190 fs). Time- versus wavelength-resolved transients were corrected for chirp and analyzed with the Surface Xplorer software (Ultrafast Systems). Laser (pump) fluence was estimated to be $20~\mu J$ cm $^{-2}$ with the pump average power measured by a Ophir PD 300 power meter diode and the beam size by a Ophir SP920S beam profiling camera using the BeamGage software.

Device fabrication

ITO-coated glass substrates (10 Ohm sq $^{-1}$ ITO, Colorado Concept Coatings) were cut into 15 \times 15 mm size pieces and cleaned via ultrasonication for 15 min in detergent in Millipore deionized water, acetone, and isopropanol in sequence. The cleaned substrates were treated with oxygen plasma at 100 W for 10 min. The PEDOT:PSS (AI 4083, Heraeus Clevios) solution was filtered with a 0.45 μ m nylon filter. A 70 μ L drop of PEDOT:PSS was spin coated on a cleaned ITO-coated glass substrate at 4,500 rpm for 45 s and annealed at 145°C for 20 min in air. The substrates

Cell Reports Physical Science

Article



were transferred to a N_2 glovebox to make 2D tin perovskite films. The 2D tin perovskite films were fabricated as mentioned previously on top of PEDOT:PSS. An ICBA solution (18 mg/mL in chlorobenzene) was then spin coated on the perovskite film at 1,000 rpm for 40 s and dried with 70° C annealing for 10 min. A BCP solution (0.5 mg/mL in isopropanol) was then spin coated on the film at 4,000 rpm for 60 s and dried without annealing. Finally, a mask was placed in front of the substrates that were loaded into a thermal evaporation chamber to thermally deposit 100 nm of silver as electrodes in a high-vacuum evaporator (<1 × 10^6 Torr). The resulting device has an area of 0.05 cm² (0.25 × 0.2 cm²) with a structure of ITO/PEDOT:PSS/quasi-2D tin perovskite/ICBA/BCP/Aq.

Electron-only and hole-only devices were fabricated as the aforementioned solar cell devices. The electron-only devices have the structure of ITO/ICBA/perovskite/ICBA/Ag with ICBA on both sides of the perovskite layer as electron transport layers. The hole-only devices have the structure of ITO/PEDOT:PSS/perovskite/PTAA/Ag. The PTAA layer was fabricated by spin-coating a 2.5 mg/mL PTAA in CB solution at 4,000 rpm for 30 s onto the perovskite layer and annealing at 100°C for 10 min.

Device characterization

The photocurrent density-voltage (J-V) curves, light-intensity-dependent J-V curves, and dark-current J-V measurements were conducted in a N_2 glovebox with an SS-F5-3A Solar Simulator provided by Enlitech. The devices were measured in reverse scan (0.8 to -0.1 V, step 0.01 V) or forward scan (-0.10 to 0.8 V, step 0.01 V) with a delay time of 30 ms. The J-V curves for all devices were measured by masking the active area using a metal mask with an area of 0.03 cm². Device contact area is 0.044 cm², which is defined by the overlap area of metal electrode and bottom ITO pattern. Before measurements, the light intensity was calibrated to 100 mW cm² using a standardized National Renewable Energy Laboratory calibrated silicon solar cell. The EQE spectra were measured using EnliTech QE-RX system.

SUPPLEMENTAL INFORMATION

Supplemental information can be found online at https://doi.org/10.1016/j.xcrp. 2022.101060.

ACKNOWLEDGMENTS

This work was financially supported by the National Science Foundation (NSF) (ECCS-2054942 and EPM-2114350). This work made use of the Cornell Center for Materials Research Shared Facilities, which are supported through the NSF MRSEC program (DMR-1719875), and the GIWAXS and TA spectroscopy from the resources of the Center for Functional Nanomaterials and the CMS beamline (11-BM) of the National Synchrotron Light Source II, both supported by US DOE Office of Science Facilities at Brookhaven National Laboratory under contract no. DE-SC0012704.

AUTHOR CONTRIBUTIONS

Conceptualization, H.L. and Q.Y.; methodology, H.L. and Q.Y.; investigation, H.L. and Q.Y.; TA measurements, H.L., Y.X., and M.C.; GIWAXS measurements, H.L., Y.X., and Y.Z.; AFM and UV stability measurements, T.L.X.; data analysis, H.L. and Q.Y.; writing – original draft, H.L.; writing – review & editing, H.L., Y.X., S.R., Y.Z., M.C., T.L.X., and Q.Y.; funding acquisition, Q.Y.

DECLARATION OF INTERESTS

The authors declare no competing interests.



Cell Reports Physical Science Article

INCLUSION AND DIVERSITY

While citing references scientifically relevant for this work, we also actively worked to promote gender balance in our reference list. We avoided "helicopter science" practices by including the participating local contributors from the region where we conducted the research as authors on the paper.

Received: April 10, 2022 Revised: July 9, 2022 Accepted: August 30, 2022 Published: September 20, 2022

REFERENCES

- Kojima, A., Teshima, K., Shirai, Y., and Miyasaka, T. (2009). Organometal halide perovskites as visible-light sensitizers for photovoltaic cells. J. Am. Chem. Soc. 131, 6050–6051.
- Min, H., Lee, D.Y., Kim, J., Kim, G., Lee, K.S., Kim, J., Paik, M.J., Kim, Y.K., Kim, K.S., Kim, M.G., et al. (2021). Perovskite solar cells with atomically coherent interlayers on SnO₂ electrodes. Nature 598, 444–450.
- 3. Dou, B., Whitaker, J.B., Bruening, K., Moore, D.T., Wheeler, L.M., Ryter, J., Breslin, N.J., Berry, J.J., Garner, S.M., Barnes, F.S., et al. (2018). Roll-to-roll printing of perovskite solar cells. ACS Energy Lett. 3, 2558–2565.
- Nasti, G., and Abate, A. (2020). Tin halide perovskite (ASnX₃) solar cells: a comprehensive guide toward the highest power conversion efficiency. Adv. Energy Mater. 10, 1902467.
- Espinosa, N., Serrano-Luján, L., Urbina, A., and Krebs, F.C. (2015). Solution and vapour deposited lead perovskite solar cells: ecotoxicity from a life cycle assessment perspective. Sol. Energy Mater. Sol. Cells 137, 303–310.
- 6. Chen, M., Ju, M.G., Garces, H.F., Carl, A.D., Ono, L.K., Hawash, Z., Zhang, Y., Shen, T., Qi, Y., Grimm, R.L., et al. (2019). Highly stable and efficient all-inorganic lead-free perovskite solar cells with native-oxide passivation. Nat. Commun. 10, 16.
- Li, X., Li, B., Chang, J., Ding, B., Zheng, S., Wu, Y., Yang, J., Yang, G., Zhong, X., and Wang, J. (2018). (C₆H₅CH₂NH₃) ₂CuBr₄: a lead-free, highly stable two-dimensional perovskite for solar cell applications. ACS Appl. Energy Mater. 1, 2709–2716.
- 8. Adonin, S.A., Frolova, L.A., Sokolov, M.N., Shilov, G.V., Korchagin, D.V., Fedin, V.P., Aldoshin, S.M., Stevenson, K.J., and Troshin, P.A. (2018). Antimony (V) complex halides: lead-free perovskite-like materials for hybrid solar cells. Adv. Energy Mater. 8, 1870026.
- Hu, W., He, X., Fang, Z., Lian, W., Shang, Y., Li, X., Zhou, W., Zhang, M., Chen, T., Lu, Y., et al. (2020). Bulk heterojunction gifts bismuthbased lead-free perovskite solar cells with record efficiency. Nano Energy 68, 104362.
- Stoumpos, C.C., Malliakas, C.D., and Kanatzidis, M.G. (2013). Semiconducting tin and lead iodide perovskites with organic cations: phase transitions, high mobilities, and

- near-infrared photoluminescent properties. Inorg. Chem. *52*, 9019–9038.
- Hao, F., Stoumpos, C.C., Cao, D.H., Chang, R.P.H., and Kanatzidis, M.G. (2014). Lead-free solid-state organic–inorganic halide perovskite solar cells. Nat. Photonics 8, 489–494.
- Jeon, I., Kim, K., Jokar, E., Park, M., Lee, H.W., and Diau, E.W.G. (2021). Environmentally compatible lead-free perovskite solar cells and their potential as light harvesters in energy storage systems. Nanomaterials 11, 2066.
- Diau, E.W.-G., Jokar, E., and Rameez, M. (2019). Strategies to improve performance and stability for tin-based perovskite solar cells. ACS Energy Lett. 4, 1930–1937.
- 14. Wang, K., Li, Z., Zhou, F., Wang, H., Bian, H., Zhang, H., Wang, Q., Jin, Z., Ding, L., and Liu, S.F. (2019). Ruddlesden-Popper 2D component to stabilize \(\gamma \cdot \ccop \ccop \sets \) perovskite phase for stable and efficient photovoltaics. Adv. Energy Mater. 9, 1902529.
- Luo, S.-Q., Wang, J.-F., Yang, B., and Yuan, Y.-B. (2019). Recent advances in controlling the crystallization of two-dimensional perovskites for optoelectronic device. Front. Phys. (Beijing). 14, 53401.
- Ortiz-Cervantes, C., Carmona-Monroy, P., and Solis-Ibarra, D. (2019). Two-dimensional halide perovskites in solar cells: 2D or not 2D? ChemSusChem 12, 1560–1575.
- Pitaro, M., Tekelenburg, E.K., Shao, S., and Loi, M.A. (2022). Tin halide perovskites: from fundamental properties to solar cells. Adv. Mater. 34, 2105844.
- Jokar, E., Chien, C.-H., Fathi, A., Rameez, M., Chang, Y.-H., and Diau, E.W.G. (2018). Slow surface passivation and crystal relaxation with additives to improve device performance and durability for tin-based perovskite solar cells. Energy Environ. Sci. 11, 2353–2362.
- Wang, F., Jiang, X., Chen, H., Shang, Y., Liu, H., Wei, J., Zhou, W., He, H., Liu, W., and Ning, Z. (2018). 2D-Quasi-2D-3D Hierarchy structure for tin perovskite solar cells with enhanced efficiency and stability. Joule 2, 2732–2743.
- Shao, S., Liu, J., Portale, G., Fang, H.-H., Blake, G.R., ten Brink, G.H., Koster, L.J.A., and Loi, M.A. (2018). Highly reproducible Sn-based hybrid perovskite solar cells with 9% efficiency. Adv. Energy Mater. 8, 1702019.

- Huang, W., Bu, T., Huang, F., and Cheng, Y.-B. (2020). Stabilizing high efficiency perovskite solar cells with 3D-2D heterostructures. Joule 4, 975–979.
- Zhang, T., Long, M., Qin, M., Lu, X., Chen, S., Xie, F., Gong, L., Chen, J., Chu, M., Miao, Q., et al. (2018). Stable and efficient 3D-2D perovskite-perovskite planar heterojunction solar cell without organic hole transport layer. Joule 2, 2706–2721.
- Liao, M., Yu, B.B., Jin, Z., Chen, W., Zhu, Y., Zhang, X., Yao, W., Duan, T., Djerdj, I., and He, Z. (2019). Efficient and stable FASnl₃ perovskite solar cells with effective interface modulation by low-dimensional perovskite layer. ChemSusChem 12, 5007–5014.
- 24. Chen, M., Dong, Q., Eickemeyer, F.T., Liu, Y., Dai, Z., Carl, A.D., Bahrami, B., Chowdhury, A.H., Grimm, R.L., Shi, Y., et al. (2020). High-performance lead-free solar cells based on tinhalide perovskite thin films functionalized by a divalent organic cation. ACS Energy Lett. 5, 2223–2230.
- Xiao, M., Gu, S., Zhu, P., Tang, M., Zhu, W., Lin, R., Chen, C., Xu, W., Yu, T., and Zhu, J. (2018). Tin-based perovskite with improved coverage and crystallinity through tin-fluoride-assisted heterogeneous nucleation. Adv. Opt. Mater. 6, 1700615.
- 26. Kumar, M.H., Dharani, S., Leong, W.L., Boix, P.P., Prabhakar, R.R., Baikie, T., Shi, C., Ding, H., Ramesh, R., Asta, M., et al. (2014). Lead-free halide perovskite solar cells with high photocurrents realized through vacancy modulation. Adv. Mater. 26, 7122–7127.
- Zhu, Z., Chueh, C., Li, N., Mao, C., and Jen, A.K. (2018). Realizing efficient lead-free formamidinium tin triiodide perovskite solar cells via a sequential deposition route. Adv. Mater. 30, 1703800.
- Wang, T., Tai, Q., Guo, X., Cao, J., Liu, C.-K., Wang, N., Shen, D., Zhu, Y., Lee, C.-S., and Yan, F. (2020). Highly air-stable tin-based perovskite solar cells through grain-surface protection by gallic acid. ACS Energy Lett. 5, 1741–1749.
- 29. Tai, Q., Guo, X., Tang, G., You, P., Ng, T.W., Shen, D., Cao, J., Liu, C.K., Wang, N., Zhu, Y., et al. (2019). Antioxidant grain passivation for air-stable tin-based perovskite solar cells. Angew. Chem. Int. Ed. Engl. 58, 806–810.
- 30. Cao, D.H., Stoumpos, C.C., Yokoyama, T., Logsdon, J.L., Song, T.-B., Farha, O.K.,

Article



- Wasielewski, M.R., Hupp, J.T., and Kanatzidis, M.G. (2017). Thin films and solar cells based on semiconducting two-dimensional Ruddlesden–Popper (CH₃(CH₂)₃NH₃)₂ (CH₃NH₃)_{n-1}Sn_nI_{3n+1} perovskites. ACS Energy Lett. 2, 982–990.
- Xu, H., Jiang, Y., He, T., Li, S., Wang, H., Chen, Y., Yuan, M., and Chen, J. (2019). Orientation regulation of tin-based reduced-dimensional perovskites for highly efficient and stable photovoltaics. Adv. Funct. Mater. 29, 1807696.
- Qiu, J., Xia, Y., Zheng, Y., Hui, W., Gu, H., Yuan, W., Yu, H., Chao, L., Niu, T., Yang, Y., et al. (2019). 2D Intermediate suppression for efficient Ruddlesden–Popper (RP) phase leadfree perovskite solar cells. ACS Energy Lett. 4, 1513–1520.
- Jiang, X., Li, H., Zhou, Q., Wei, Q., Wei, M., Jiang, L., Wang, Z., Peng, Z., Wang, F., Zang, Z., et al. (2021). One-step synthesis of Snl₂. (DMSO)_x adducts for high-performance tin perovskite solar cells. J. Am. Chem. Soc. 143, 10970–10976.
- 34. Liang, C., Gu, H., Xia, Y., Wang, Z., Liu, X., Xia, J., Zuo, S., Hu, Y., Gao, X., Hui, W., et al. (2020). Two-dimensional Ruddlesden–Popper layered perovskite solar cells based on phase-pure thin films. Nat. Energy 6, 38–45.
- Jeong, J., Kim, M., Seo, J., Lu, H., Ahlawat, P., Mishra, A., Yang, Y., Hope, M.A., Eickemeyer, F.T., Kim, M., et al. (2021). Pseudo-halide anion engineering for alpha-FAPbl₃ perovskite solar cells. Nature 592, 381–385.
- 36. Wang, J., Shen, H., Li, W., Wang, S., Li, J., and Li, D. (2019). The role of chloride incorporation in lead-free 2D perovskite (BA)₂Snl₄: morphology, photoluminescence, phase transition, and charge transport. Adv. Sci. 6, 1802019.
- Dong, H., Ran, C., Gao, W., Sun, N., Liu, X., Xia, Y., Chen, Y., and Huang, W. (2022). Crystallization dynamics of Sn-based perovskite thin films: toward efficient and stable photovoltaic devices. Adv. Energy Mater. 12, 2102213.
- 38. Qiu, J., Lin, Y., Ran, X., Wei, Q., Gao, X., Xia, Y., Müller-Buschbaum, P., and Chen, Y. (2021). Efficient and stable Ruddlesden-Popper layered tin-based perovskite solar cells enabled by ionic liquid-bulky spacers. Sci. China Chem. *64*, 1577–1585.
- Gu, H., Niu, T., Zuo, S., Cai, Y., Chao, L., Müller-Buschbaum, P., Xia, Y., Zhang, J., Xing, G., and Chen, Y. (2022). Stable metal-halide perovskite colloids in protic ionic liquid. CCS Chem. 1–11. https://doi.org/10.31635/ccschem.022. 202101629.
- Hui, W., Chao, L., Lu, H., Xia, F., Wei, Q., Su, Z., Niu, T., Tao, L., Du, B., Li, D., et al. (2021). Stabilizing black-phase formamidinium perovskite formation at room temperature and high humidity. Science 371, 1359–1364.

- 41. Walker, B., Kim, G.H., and Kim, J.Y. (2019). Pseudohalides in lead-based perovskite semiconductors. Adv. Mater. 31, 1807029.
- Lin, P., Loganathan, A., Raifuku, I., Li, M., Chiu, Y., Chang, S., Fakharuddin, A., Lin, C., Guo, T., Schmidt-Mende, L., et al. (2021). Pseudo-halide perovskite solar cells. Adv. Energy Mater. 11, 2100818.
- Zhang, W., Wu, X., Zhou, J., Han, B., Liu, X., Zhang, Y., and Zhou, H. (2022). Pseudohalideassisted growth of oriented large grains for high-performance and stable 2D perovskite solar cells. ACS Energy Lett. 7, 1842–1849.
- 44. Tosado, G.A., Zheng, E., and Yu, Q. (2020). Tuning cesium-guanidinium in formamidinium tin triiodide perovskites with an ethylenediammonium additive for efficient and stable lead-free perovskite solar cells. Mater. Adv. 1, 3507–3517.
- Yan, L., Hu, J., Zhou, N., Moran, A.M., and You, W. (2019). Enhancing photovoltaic performance of aromatic ammonium-based two-dimensional organic-inorganic hybrid perovskites via tuning CH, π interaction. Sol. RRL 4, 1900374.
- Gao, C., Hu, Z., Yang, C., Xu, H., Wang, Y., Zhang, J., and Zhu, Y. (2019). Threedimensional perovskite modulated by twodimensional homologue as light-absorbing materials for efficient solar cells. Org. Electron. 74, 126–134.
- Li, N., Zhu, Z., Dong, Q., Li, J., Yang, Z., Chueh, C.-C., Jen, A.K.Y., and Wang, L. (2017). Enhanced moisture stability of cesiumcontaining compositional perovskites by a feasible interfacial engineering. Adv. Mater. Interfaces 4, 1700598.
- 48. Wu, T., Wang, Y., Li, X., Wu, Y., Meng, X., Cui, D., Yang, X., and Han, L. (2019). Efficient defect passivation for perovskite solar cells by controlling the electron density distribution of donor-π-acceptor molecules. Adv. Energy Mater. 9, 1803766.
- Wu, T., Wang, Y., Dai, Z., Cui, D., Wang, T., Meng, X., Bi, E., Yang, X., and Han, L. (2019). Efficient and stable CsPbl₃ solar cells via regulating lattice distortion with surface organic terminal groups. Adv. Mater. 31, 1900.015
- Fan, J., Ma, Y., Zhang, C., Liu, C., Li, W., Schropp, R.E.I., and Mai, Y. (2018). Thermodynamically self-healing 1D–3D hybrid perovskite solar cells. Adv. Energy Mater. 8, 1703421.
- Li, F., Zhang, C., Huang, J.H., Fan, H., Wang, H., Wang, P., Zhan, C., Liu, C.M., Li, X., Yang, L.M., et al. (2019). A cation-exchange approach for the fabrication of efficient methylammonium tin iodide perovskite solar cells. Angew. Chem., Int. Ed. 58, 6688–6692.

- Qing, J., Liu, X.-K., Li, M., Liu, F., Yuan, Z., Tiukalova, E., Yan, Z., Duchamp, M., Chen, S., Wang, Y., et al. (2018). Aligned and graded type-II Ruddlesden-Popper perovskite films for efficient solar cells. Adv. Energy Mater. 8, 1800185.
- Liu, J., Leng, J., Wu, K., Zhang, J., and Jin, S. (2017). Observation of internal photoinduced electron and hole separation in hybrid twodimentional perovskite films. J. Am. Chem. Soc. 139, 1432–1435.
- Proppe, A.H., Quintero-Bermudez, R., Tan, H., Voznyy, O., Kelley, S.O., and Sargent, E.H. (2018). Synthetic control over quantum well width distribution and carrier migration in lowdimensional perovskite photovoltaics. J. Am. Chem. Soc. 140, 2890–2896.
- Bube, R.H. (1962). Trap density determination by space-charge-limited currents. J. Appl. Phys. 33, 1733–1737.
- Qiu, J., Xia, Y., Chen, Y., and Huang, W. (2019). Management of crystallization kinetics for efficient and stable low-dimensional Ruddlesden-Popper (LDRP) lead-free perovskite solar cells. Adv. Sci. 6, 1800793.
- Liu, C., Tu, J., Hu, X., Huang, Z., Meng, X., Yang, J., Duan, X., Tan, L., Li, Z., and Chen, Y. (2019). Enhanced hole transportation for inverted tinbased perovskite solar cells with high performance and stability. Adv. Funct. Mater. 29, 1970117.
- Cowan, S.R., Roy, A., and Heeger, A.J. (2010). Recombination in polymer-fullerene bulk heterojunction solar cells. Phys. Rev. B 82, 245207
- Proctor, C.M., and Nguyen, T.-Q. (2015). Effect of leakage current and shunt resistance on the light intensity dependence of organic solar cells. Appl. Phys. Lett. 106, 083301.
- Jahandar, M., Khan, N., Lee, H.K., Lee, S.K., Shin, W.S., Lee, J.C., Song, C.E., and Moon, S.J. (2017). High-performance CH₃NH₃Pbl₃-inverted planar perovskite solar cells with fill factor over 83% via excess organic/ inorganic halide. ACS Appl. Mater. Interfaces 9, 35871–35879.
- 61. Jiang, X., Zang, Z., Zhou, Y., Li, H., Wei, Q., and Ning, Z. (2021). Tin halide perovskite solar cells: an emerging thin-film photovoltaic technology. Acc. Mater. Res. 2, 210–219.
- 62. Liao, Y., Liu, H., Zhou, W., Yang, D., Shang, Y., Shi, Z., Li, B., Jiang, X., Zhang, L., Quan, L.N., et al. (2017). Highly oriented low-dimensional tin halide perovskites with enhanced stability and photovoltaic performance. J. Am. Chem. Soc. 139, 6693–6699.
- Renaud, G., Lazzari, R., and Leroy, F. (2009). Probing surface and interface morphology with grazing incidence small angle X-ray scattering. Surf. Sci. Rep. 64, 255–380.